

Superior Performance of Lithium-Ion Batteries with High-Loading Graphite Anode via Dry Processible Node-Shaped Connective Binder

Jin-Wook Min, Keun-Ho Heo, Hyun-Seung Kim, Chihyun Hwang, Jong-Hyun Park, Je-Nam Lee, Ji-Sang Yu, Won-Jin Kwak, Dong-Won Kim,* Jang-Yeon Hwang,* and Yun-Chae Jung*

As the demand for high-performance energy storage solutions increases, lithium-ion batteries (LIBs) remain the leading technology in electric vehicles (EVs) and portable electronics. However, traditional wet-casting electrode (WCE) processes have inherent limitations, such as binder migration and environmental concerns associated with solvent use. In this study, a high-loading dry-casting electrode (DCE) approach is proposed to overcome these challenges by eliminating solvent use and improving electrode uniformity. The DCE, fabricated using polyvinylidene fluoride-co-hexafluoropropylene (PVdF-HFP) binder nanoparticles, improves binder distribution among the natural graphite particles, enhances lithium-ion transport, and mitigates interfacial reactions. Electrochemical analysis reveals that the DCE outperforms the WCE, particularly under high loading conditions ($\approx 7 \text{ mAh cm}^{-2}$). The pouch-type full-cell test exhibits a 67.8% capacity retention after 700 cycles, indicating stable cell cycling. Consequently, this study highlights the potential of DCE to improve capacity retention, enhance rate capability, and reduce electrode degradation for commercial applications.

(VOC) emissions generated during the battery electrode manufacturing process.^[4–6]

The conventional wet-casting process (WCP) for electrode fabrication entails the amalgamation and dispersion of active materials, conducting additives, and polymeric binders in solvents [e.g., water and N-methylpyrrolidone (NMP)].^[7–9] This method has several limitations. The prepared slurry (colloidal mixture) is gradually coated onto the current collector (copper foil for the anode and aluminum foil for the cathode), and the solvent is dried at temperatures exceeding 100 °C to form the electrode. The organic solvent NMP, which is used to dissolve the polyvinylidene fluoride (PVdF) binder in the cathodes, emits VOCs during the drying process. These VOCs are harmful to both human health and the environment. Therefore, solvents, including

NMP, need to undergo solvent recovery processes. This results in substantial energy consumption and high investment costs for drying and solvent recovery, which inevitably affect the overall cost of the cells.^[10–12] Moreover, in high-mass-loading electrodes or under rapid drying conditions, a binder concentration gradient develops within the coating layer owing to the lag in binder mass transfer during solvent evaporation.^[13] This reduces the binder content between the electrode particles.

1. Introduction

Technological advancements in lithium-ion batteries (LIBs) have enabled the development of energy storage devices characterized by high energy densities, substantial power outputs, and extended cycle lives, thereby promoting the commercialization of electric vehicles (EVs).^[1–3] However, environmental challenges arise from the substantial carbon and volatile organic compound

J.-W. Min, D.-W. Kim
Department of Chemical Engineering
Hanyang University
Seongdong-gu, Seoul 04763, Republic of Korea
E-mail: dongwonkim@hanyang.ac.kr

J.-W. Min
Battery Materials R&D Laboratory
POSCO Future M, Sejong 30002, Republic of Korea

K.-H. Heo, H.-S. Kim, C. Hwang, J.-H. Park, J.-N. Lee, J.-S. Yu, Y.-C. Jung
Advanced Batteries Research Center
Korea Electronics Technology Institute (KETI)
Seongnam-si, Gyeonggi 13509, Republic of Korea
E-mail: yunchae.jung@keti.re.kr

J.-H. Park, D.-W. Kim, J.-Y. Hwang
Department of Energy Engineering
Hanyang University
Seongdong-gu, Seoul 04763, Republic of Korea
E-mail: jangyeonhw@hanyang.ac.kr

W.-J. Kwak
School of Energy and Chemical Engineering
Ulsan National Institute of Science and Technology (UNIST)
Ulsan 44919, Republic of Korea

The ORCID identification number(s) for the author(s) of this article can be found under <https://doi.org/10.1002/adsu.202401039>

DOI: 10.1002/adsu.202401039

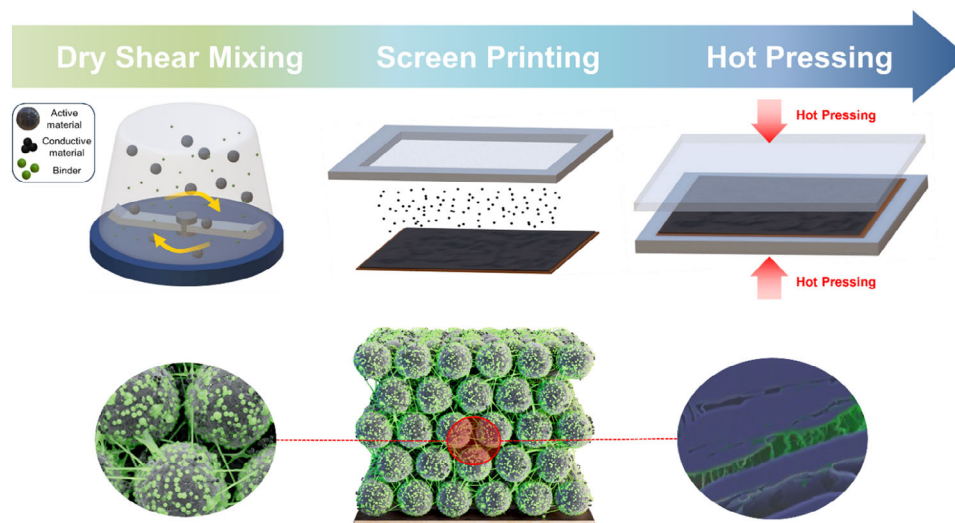


Figure 1. Schematic illustration of the DCE.

Consequently, the cohesion among the particles and adhesion between the particles and current collectors decrease, leading to degradation in the electrode quality and subsequent deterioration of battery performance.^[14–17]

The dry process is a potentially viable method for LIB manufacturing, because it enables direct fabrication without solvents, thereby addressing the abovementioned issues.^[18–20] The absence of solvents in the dry process prevents a concentration gradient of the binder in the electrode, allowing for low-cost production of high-loading electrodes. Additionally, fabricating high-loading electrodes increases the loading level of the active material by $\approx 30\%$, while the reduction in inactive components (e.g., current collectors and separators) enhances the energy density and reduces manufacturing costs.^[21,22]

Currently, research is being conducted on various types of dry processes, such as fibrillation, extrusion, CVD, and spraying.^[23–25] Among numerous polymer binders, polytetrafluoroethylene (PTFE) binders are widely used in dry processes because of their unique fibrillation properties.^[26–28] These properties enable the fabrication of electrodes without solvent. However, anodes that contain PTFE binders are prone to reduction at low potentials (≈ 1.2 V vs Li/Li⁺) because of the low LUMO level of PTFE.^[29–34] The reduction in PTFE negatively impacts the discharge capacity and coulombic efficiency. Consequently, selecting a binder that maintains electrochemical stability during the charge/discharge process is crucial to fabricate dry anodes.

In this study, we proposed dry-casting electrode (DCE) fabrication using binder nanobead-containing natural graphite. The polyvinylidene fluoride-co-hexafluoropropylene (PVdF-HFP) nanoparticles in the DCE formed node-like contacts between the graphite particles during electrode fabrication, resulting in a uniform electrode structure, adhesion strength, and void distribution across the entire electrode area. The characteristics of the DCE were compared with those of the wet-casting electrode (WCE). The DCE showed improved charging performance under highly loaded conditions (18.7 mg cm^{-2} , 6.9 mAh cm^{-2}). DCE-based pouch cells were fabricated to investigate their potential for practical applications in energy storage and battery technology.

2. Results and Discussion

The DCE was fabricated as shown in Figure 1. During the dry shear mixing step, graphite powder that had been coated with carbon black was combined with a PVdF-HFP emulsion to attach the binder nanobeads to the surface (Figure S1a–c, Supporting Information). The graphite complex in DCE exhibits a dot-like binder distribution, facilitating uniform particle dispersion and promoting node-shaped contact during electrode assembly. The graphite complex was evenly applied to the current collector, and the electrode was formed during hot pressing, which activated the adhesion of the binder. Considering that the binder in the graphite complex had a melting temperature of ≈ 140 °C (Figure S2, Supporting Information), the 150 °C conditions that were applied during hot pressing facilitated its melting and established a robust bond between the graphite and binder nanobeads in the electrode. This process enabled the production of a uniform and flexible thick-film electrode (Figure S3, Supporting Information).

The primary advantage of employing the dry process is the uniformity of the electrode. The drying conditions can lead to uneven binder distribution between the top and bottom of the electrode in the wet process, which can subsequently result in inadequate electrolyte infiltration or inconsistent adhesion strengths within the electrode.^[35] Scanning electron microscopy (SEM) cross-sectional analysis compared the binder distribution in the electrodes manufactured using the dry method and those produced utilizing the NMP-based wet process at identical loading levels (Figure 2a–f). The dry electrode exhibited a relatively uniform structure, whereas the wet electrode showed an uneven composition with the binder predominantly concentrated at the top. The dry electrodes demonstrated almost uniform pore distributions throughout the top and bottom, whereas the wet electrodes exhibited pore clustering in the binder-concentrated top region. EDS analysis reveals that in thick WCEs, binder migration causes the F element to concentrate predominantly in the top region. Rapid solvent evaporation during slurry drying leads to non-uniform binder distribution at the surface. In contrast, the F element in DCE is uniformly distributed due to the

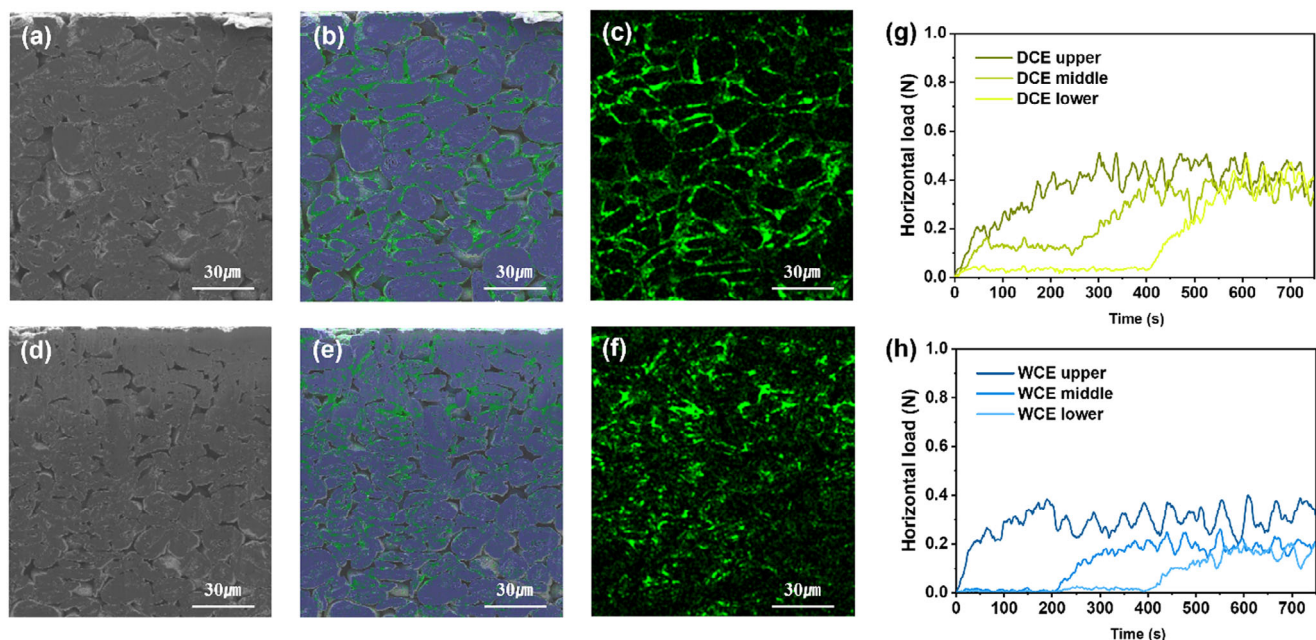


Figure 2. SEM-EDS images of electrode cross-section. Blue color indicates C element from graphite and green color shows F element from binder: a–c) DCE and d–f) WCE. SAICAS analysis of g) DCE and h) WCE with various depth positions.

pre-dispersed nanobead binder on the graphite surface. Further analysis of the active material surface indicates that in DCE, the binder connects graphite particles in a truss-like configuration, extending in a node-shaped manner as pressure is released during the pressing process (Figures S4a,b, S5a,b, Supporting Information). Conversely, in WCE, the binder merely coats the surface of the active material, leading to narrower bonding points between particles compared to DCE (Figures S4c,d, S5c,d, Supporting Information). Notably, in DCE, the binder is effectively encapsulated on the graphite surface, whereas in WCE, it infiltrates graphite pores and accumulates within the electrode. This indicates that in the wet process, the binder—crucial for maintaining particle cohesion—is unnecessarily distributed within the electrode rather than forming strong interparticle connections. Consequently, unwanted resistance could result in areas where contact between the electrolyte and electrode occurred, potentially leading to inefficiencies. This was verified by comparing the resistivities of the electrodes (Table S1, Supporting Information). Moreover, SEM image of the electrode structure highlights that difference in binder distribution between dry and wet electrodes influence key properties such as adhesion, cohesion strength, pore distribution, and wettability.

The adhesion strengths of the electrodes at different positions were measured using the surface and interfacial cutting analysis system (SAICAS) (Figure 2g,h), with measurements performed at the upper (25%), middle (50%), and lower (75%) positions along the thickness of the electrode. The conventional peel test, which employs tape to measure adhesion strength, is effective; however, it measures the force for delamination at the weakest point within the electrode. Therefore, it may not provide a comprehensive understanding of the overall adhesion strength of the electrode. However, SAICAS enabled us to precisely analyze the differences in the adhesion strength along the thickness direc-

tion, providing valuable insights into the overall adhesion properties of the electrode.^[36] The horizontal force recorded at a specified depth revealed that the adhesion strength of the dry electrode surpassed that of the wet electrode. This was because the binder was solely used to accurately bind the active material during the dry process. Furthermore, the dry electrode exhibited consistent adhesion strength, whereas the wet electrode showed increased adhesion strength at the top and decreased strength toward the bottom. This was closely related to the binder distribution within the wet electrode, where the binder was predominantly concentrated at the top. Therefore, the binder was less involved in electrode bonding toward the bottom. To confirm the structural stability of the electrode, the dry and wet electrodes were immersed in a liquid electrolyte and subjected to ultrasonication for 5 min (Figure S6, Supporting Information). Consequently, the dry electrode predominantly retained its initial shape with minimal detachment, whereas the wet electrode completely disintegrated and dispersed into the electrolyte. As indicated in the SAICAS evaluation, the dry electrode exhibited superior inter-particle adhesion.

To elucidate the internal characteristics of the electrodes, the dry and wet electrodes were comparatively analyzed using X-ray microscopy (XRM). The generated XRM images were 3D-reconstructed to analyze the inner framework and distribution of the components and pores.^[37,38] Specifically, XRM pore analysis (Figure 3a–c) provides quantitative insights into these differences. The dry electrode (DCE) exhibits large and uniformly distributed pores throughout, whereas the wet electrode (WCE) shows a higher concentration of large pores at the top (yellow-red region). The pore content analysis reveals that DCE has an overall pore content of 10.7%, while WCE has 7.9%. Moreover, in DCE, the pore content remains relatively stable between the top (12%) and bottom (10%) regions. In contrast, WCE

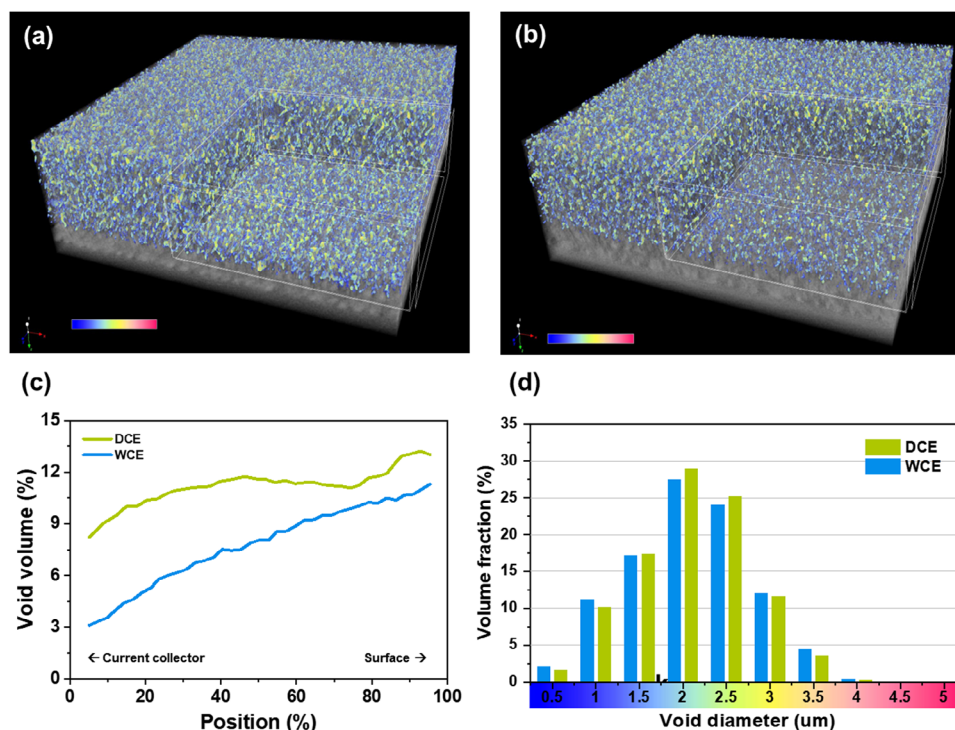


Figure 3. 3D-reconstructed images from X-ray microscope: a) DCE and b) WCE. c) Void fraction of electrode calculated and d) Void distribution in electrode from 3D-reconstructed images.

demonstrates a more pronounced gradient, with 10% pore content at the top and only 4.7% at the bottom. The differences in pore content between the top and bottom regions measure 2% for DCE and 5.3% for WCE, reinforcing the observation that WCE exhibits a non-uniform pore distribution that negatively impacts ion transport and overall electrochemical performance. An analysis of the pore size distribution revealed that, while the average pore sizes of the dry and wet electrodes were similar, the deviation in pore size was larger in the wet electrode than in the dry electrode (Figure 3d). Binder aggregation in the upper layer inevitably affected the electrolyte infiltration capability when applied to batteries.^[39]

Contact angle measurements were conducted to verify the electrolyte wettability (Figure S7, Supporting Information). The initial contact angle of the dry electrode was smaller than that of the wet electrode (26° vs 32°), and the liquid electrolyte completely infiltrated the dry electrode within 5 s. In contrast, the liquid electrolyte did not penetrate the wet electrode even after 10 s. These results indicate that the dry electrode can achieve uniform and sufficient conductive pathways within the battery, thereby demonstrating its superior conductive properties.^[40] Differences due to binders could be observed at the electrode and interparticle levels. When conducting the BET surface area analysis (Figure S8, Supporting Information), the DCE exhibited a value ($3.02 \text{ m}^2 \text{ g}^{-1}$) similar to graphite powder ($3.33 \text{ m}^2 \text{ g}^{-1}$), whereas the WCE showed reduced surface area ($2.38 \text{ m}^2 \text{ g}^{-1}$). This phenomenon could be attributed to binders covering the graphite particles during the WCE. Conversely, the graphite surface is well maintained owing to the node-shaped contact in dry processes. Because of minimal pore clogging by dry-processable binders,

the DCE exhibited superior lithium intercalation/deintercalation characteristics and was considered kinetically advantageous.^[41,42]

Figure 3 illustrates the electrochemical and spectroscopic characterization of the DCE and WCE in terms of the negative electrode ($\approx 7 \text{ mAh cm}^{-2}$, Figure 4a) and full-cell levels. Figure 4b shows the cyclic voltammograms of the DCE and WCE in the Li half-cell configuration. Because identical scan rates and active materials were applied to compare the generated current and peak voltages during the voltage sweep, the polarization from the DCE and WCE could be directly compared with the cyclic voltammograms. The cathodic and anodic peak potentials were observed at 0.09 and 0.33 V (vs Li/Li⁺) and 0.08 and 0.43 V (vs Li/Li⁺) for DCE and WCE, respectively; therefore, the polarization developed during the electrode redox reaction was significantly reduced with DCE architecture. The homogeneously distributed binder from the sophisticated electrode fabrication process greatly influenced the electrode kinetics.^[43,44] The graphite-electrolyte interface was effectively formed with optimal electrolyte soaking and minimal dead volume due to binder agglomeration in the electrode. To further verify the effects of the electrode fabrication process on the kinetics of the graphite negative electrodes, C-rate-dependent lithiation was performed in a half-cell configuration (Figure 4c; Figure S9, Supporting Information). The relative ratio of the CC-lithiated capacity to the overall lithiation capacity was demonstrated because the subsequent constant voltage (CV) step was applied after the end of the constant current (CC) period. During slow C-rate application, the CC-lithiation period was relatively similar for the DCE and WCE (i.e., 92.7% and 89.1% were CC-lithiated at the DCE and WCE, respectively, at 0.2 C application). In contrast, the gap between

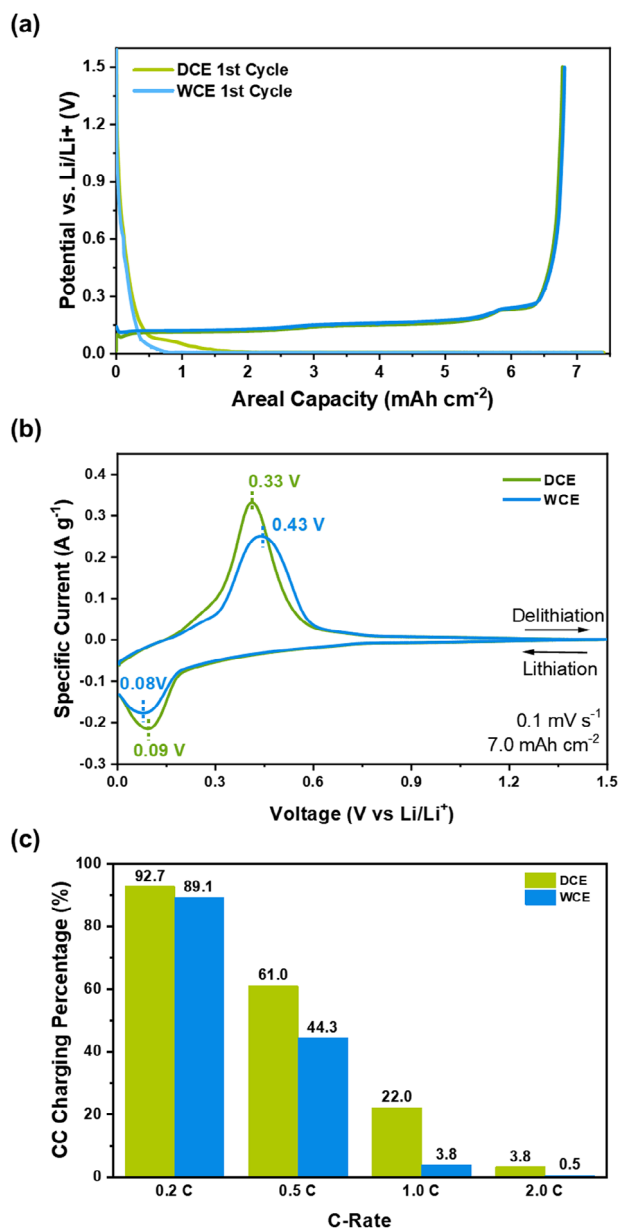


Figure 4. Electrochemical performance of DCE and WCE. a) Charge/discharge voltage profile of Half-cells at initial cycle. b) cyclic voltammogram at 0.1 mV s⁻¹. c) Ratio of CC mode charged capacity versus charged capacity at each C-rate.

the DCE and WCE was substantially increased, even at a 0.5 C-rate, resulting in a 16.7% difference. Notably, the increased CC-lithiation ratio of the graphite electrode implies reduced lithiation polarization.^[45,46] Therefore, the structural modification of the negative electrode due to changes in the fabrication process strongly influenced the lithiation kinetics of the electrode, as evidenced by the cyclic voltammetry results.

Although the binder was homogeneously distributed on the graphite surface on the DCE, locally aggregated binder was observed on the WCE. Consequently, the bare graphite edge-plane exposure to the electrolyte solution can be increased at

the WCE electrode with an identical weight percentage to the binder introduction. Therefore, a differential capacity plot was used to demonstrate the comparative reduction of ethylene carbonate (EC) during the initial formation process utilizing the graphite/LiNi_{0.8}Co_{0.1}Mn_{0.1}O₂ (NCM811) electrode-based full-cell configuration (Figure 5a). Because direct exposure of the graphite surface was suppressed by the DCE architecture, the EC reduction peaks were significantly reduced in the DCE compared with those in the WCE. The Nyquist plots (Figure 5b) indicate decreased initial resistance at the DCE compared with that at the WCE. The recorded impedance at 100 Hz, the typical frequency for the solid electrolyte interphase resistance (R_{SEI}) of a graphite electrode,^[47] indicated that the R_{SEI} was highly reduced at the DCE. Spectroscopic characterization of the solid electrolyte interphase (SEI) film deposited on the graphite electrode was performed with X-ray photoelectron spectroscopy (XPS) (Figure 5c). The relative ratios of SEI components, such as C-O, C=O, and Li₂CO₃, to the bare electrode surface, represented by lithiated graphite (Li-C), can indicate SEI film thickness. This is because the penetration depth of X-rays remains consistent during XPS measurements.^[48,49] The C 1s narrow-scanned spectra showed that the evolution of the Li-C peak, originating from the lithiated graphite, was higher at the DCE than at the WCE. This implied that the SEI was thinner at the DCE electrode. While the PVdF-HFP was gradually etched at the DCE from a homogeneous distribution, an evident PVdF peak suddenly emerged at the WCE due to the inhomogeneous binder dispersion. The development of the electrolyte-graphite interface was effectively performed at the DCE, as evidenced by the Li-half-cell evaluation; therefore, further evaluation of the full-cell configuration was conducted. The galvanostatic intermittent titration technique (GITT) facilitated the evaluation of the relative active surface area ratio in a full cell (Figure 5d; Figure S10, Supporting Information). Because the applied components, thickness, and density of the negative electrode were the same for the DCE and WCE, the obtained diffusion coefficient should be modified based on the actual contact surface area of graphite with the electrolyte. Therefore, the ratio of the estimated diffusion coefficient of the WCE was divided by that of the DCE to compare the electrolyte-active material contact ratio. Figure 5d shows that only 60% of the graphite is in effective contact with the electrolyte; therefore, the improved electrode kinetics of the DCE were because of the efficient contact between the electrolyte and the active material. This led to a high diffusion coefficient at the electrode level. Moreover, the ratio was consistently observed over a wide state-of-charge range, indicating that the results originated from the negative electrode. Based on the improved electrochemical characteristics of the DCE, the rate capability of graphite/NCM811 was substantially improved compared to that of the WCE utilized in LIBs (Figure 5e).

The durability of the DCE in the pouch-type cells was evaluated because of the enhanced physicochemical and electrochemical characteristics of the graphite electrode (Figure 6a–e). In Figure 6a, the high areal capacity DCE comprised graphite/NCM811 pouch cell exhibited enhanced cyclability compared to WCE, achieving a 67.8% (from 184.4 mAh g⁻¹ to 125.0 mAh g⁻¹) of discharge capacity retention at 700 cycles. In contrast, WCE, despite utilizing similar materials, retained only 16.6% of its discharge capacity after 700 cycles (from 185 mAh g⁻¹ to 30.7 mAh g⁻¹). This was attributed to the high diffusion

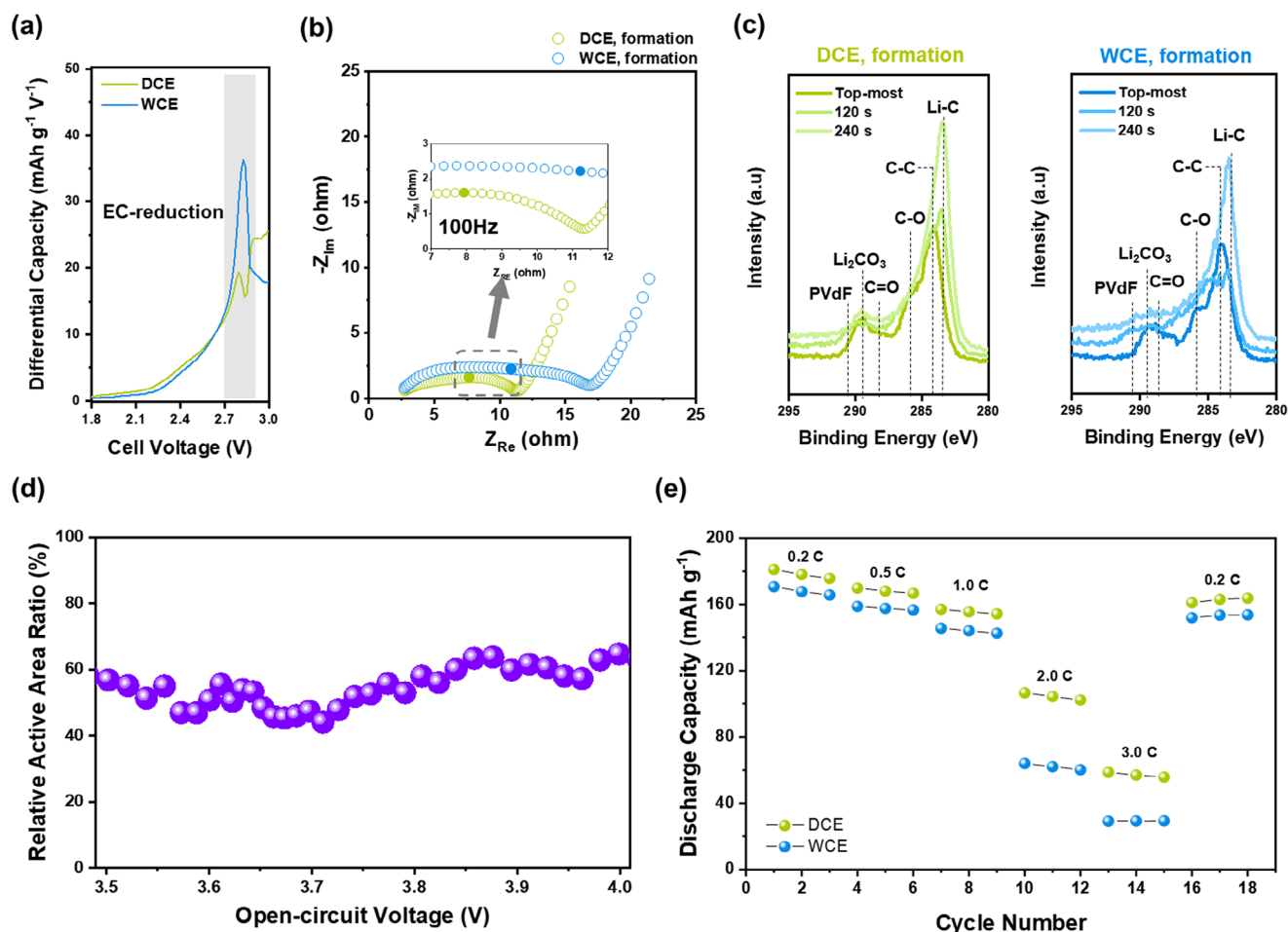


Figure 5. Electrochemical performance of full cell DCE and WCE. a) dQ/dV analysis at initial charging step with graphite/NCM811 configuration. b) the Nyquist plots of full cells after formation. c) XPS spectra of graphite electrodes after formation. d) relative active surface area ratio calculated from GITT analysis. e) Full-cell rate capability at C-rates from 0.2 C to 3 C charge.

coefficient resulting from the increased graphite-electrolyte contact and the decreased cathodic side reaction due to the reduced direct exposure of the graphite surface to the electrolyte without binder. Consequently, the effective employment of active material can be achieved using the DCE fabrication method. The post-mortem C 1s XPS spectra indicated a decrease in additional SEI deposition at the DCE due to the inhibition of direct graphite exposure to the electrolyte, as evidenced by the Li-C peak intensity. As shown in Figure 6b, a higher Li-C peak intensity was observed for the DCE than for the WCE after the 700th cycle. The impedance was measured post-cycling and represented as Nyquist plots (Figure 6c). The terminal impedances of the pouch cells indicated that the R_{DCE} was significantly lower than the R_{WCE} due to less electrolyte decomposition. The nominal voltage variation during the cycle (Figure 6d) indicated that the developed polarization of the cell was well maintained at the DCE, while the WCE suffered significantly increased overpotential during the cycle because of further side reactions and mechanical deterioration of the graphite electrode. The cycle-number-dependent voltage profiles evidently correlate with the Nyquist plots and nominal voltage variation (Figure 6e; Figure and S11, Supporting In-

formation). The capacity decay-coupled polarization growth was considerably mitigated by DCE application, whereas the WCE struggled with increased polarizations due to side reactions.

Based on our previous investigations, we illustrated graphite electrodes with different preparations (DCE and WCE) and the effects of the electrode fabrication process in Figure 7. Although similar binder was used, the differences in the configuration of the graphite and binder, because of the proven variations, had a significant impact on the electrode morphology and cell performance. The uneven distribution caused by binder migration in the WCE resulted in an accumulation of binder in the upper region, obstructing the lithium pathway and limiting the kinetics. In the lower region of the WCE, insufficient binder coverage on graphite led to significant exposure of the graphite surface, promoting side reactions with the electrolyte. In contrast to the wet process, the DCE formed efficient and uniform node-shaped adhesions across the entire electrode, ensuring sufficient lithium-ion transport pathways and mitigating interfacial side reactions between the graphite and liquid electrolyte. Consequently, the graphite anode dry process demonstrates the ability to produce high-performance LIBs with high energy densities.

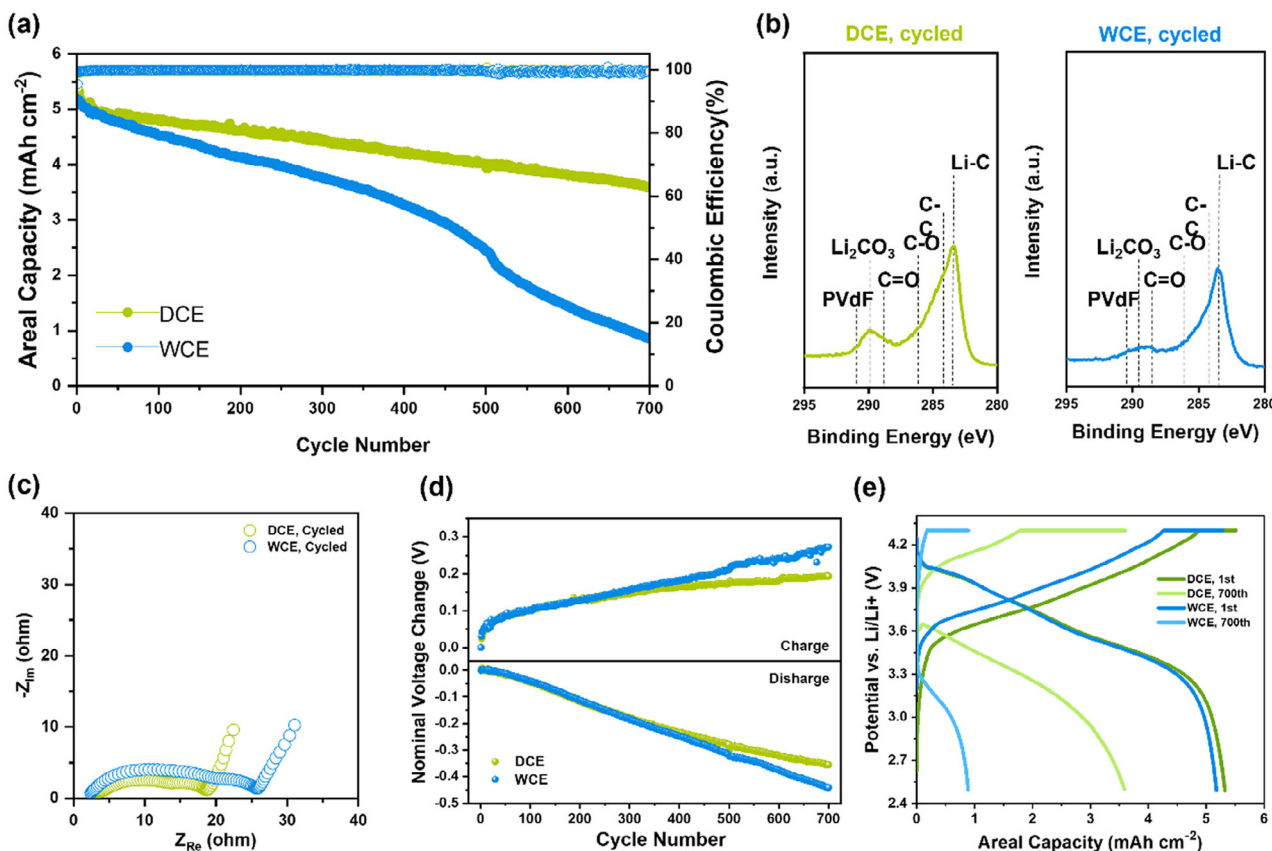


Figure 6. a) Cycle performance in the voltage range 2.5–4.3 V at 0.5 C and digital image (inner). b) XPS spectra of graphite electrodes after cycling. c) Nyquist plots of full cells after cycle. d) Comparison of nominal voltage change and e) capacity-voltage profiles of full cells at initial and 700th cycle.

3. Conclusion

In this study, we proposed a high-loading DCE process with a PVDF-HFP binder for LIB fabrication to address the key challenges associated with the wet process, such as solvent use, binder migration, and environmental and cost concerns. By uniformly distributing the binder across the graphite particles as nodes, DCE enhanced the lithium-ion transport and reduced the interfacial reactions, resulting in superior electrochemical performance. Full-cell testing confirmed that the DCE-based electrodes exhibited superior capacity retentions and cycling stabilities under high loading conditions compared to the WCE. The environmental and performance advantages of the DCE highlight its potential use in high-energy-density LIBs, particularly in EVs and other energy storage applications. Future research should investigate further optimizations of the binder materials and electrode configurations to push the limits of battery performance.

4. Experimental Section

Preparation of the Electrodes: The DCE powder was sequentially coated on the surface of natural graphite (POSCO FUTURE M Co., Ltd.) through dry shear mixing with carbon black (Super P, Imerys G&C Ltd.) and PVDF-HFP emulsion in de-ionized water (Solvay Specialty Polymers Korea Co., Ltd.) in a weight ratio of 93:1:6. Shear mixing enabled uniform coating by directly attaching nanoparticles to the surface of the active material,

offering a more uniform coating compared to wet casting process. The shear-mixed sample was fully dried in an oven at 80 °C, and then deagglomerated using a mortar. The prepared graphite complex was dispersed and deposited onto copper foil through a mesh screen. Before hot pressing, a paper film was placed over the graphite complex powder to prevent it from sticking to the steel plate and the electrode. The prepared sample was then pressed at 150 °C for 5 min under a load of 250 bar (17 MPa) and subsequently adjusted to the desired thickness and density through roll pressing at room temperature. On the other hand, the SCE anode was prepared using the same graphite and carbon black as in the DCE, but with polyvinylidene fluoride (PVDF, Solvay Specialty Polymers Korea Co., Ltd.) as a binder solution in NMP, maintaining the same weight ratio as the DCE. The slurry was pre-mixed using a Thinky mixer (ARE-310, THINKY Corporation) at 1000 rpm for 5 min, followed by main mixing at 2000 rpm for 10 min, and then coated onto the Cu current collector using a doctor blade. After coating, the casted electrode was dried in an oven at 80 °C for 2 h, followed by vacuum drying at 120 °C for 10 h, and the desired thickness and density were controlled through roll pressing. For the evaluation of the full cell, a dry cathode electrode was used as the counter electrode. The LiNi_{0.8}Co_{0.1}Mn_{0.1}O₂ (NCM811, POSCO FUTURE M Co., Ltd.), carbon nanofiber (CNF, MERCK), and PTFE binder (Solvay Specialty Polymers Korea Co., Ltd.) were mixed in a weight ratio of 95:3:2 through dry shear mixing, and then processed into a freestanding electrode using a pasta machine. This freestanding cathode was laminated onto a 15 μm aluminum current collector at room temperature through roll pressing, adjusted to match the N/P ratio of the graphite anode.

Preparation of the Electrodes: The morphology of the conductive material and binder nanoparticles coated on the graphite surface, along with the graphite complex, was observed using a field-emission scanning electron microscope (FE-SEM, GeminiSEM 460, ZEISS) combined with an

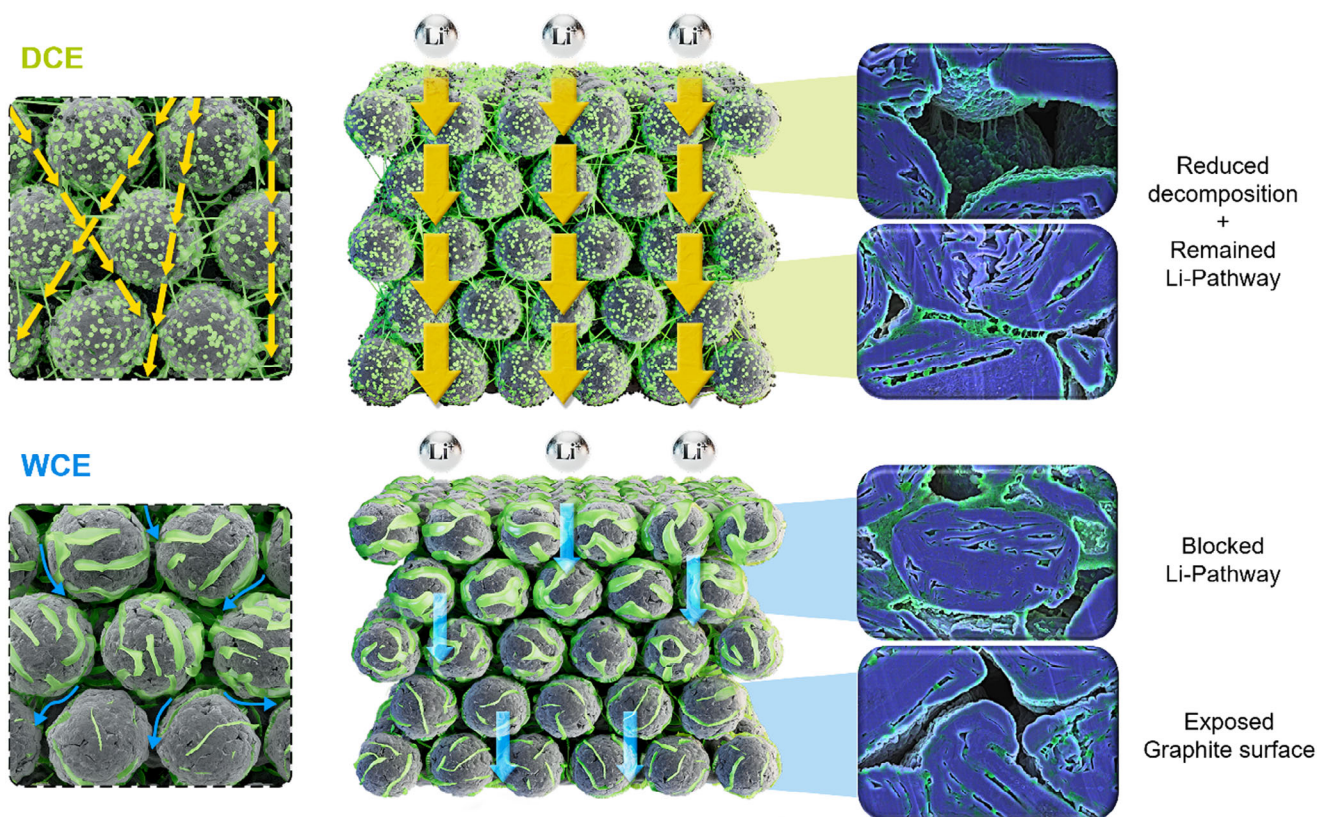


Figure 7. Schematic illustration of morphology and following Li ion diffusion difference between DCE and WCE.

energy-dispersive X-ray spectrometer (EDS, ULTIM EXTREME, Oxford instruments). The graphite electrode was cut for 10 h at a 5.5 kV beam using a cross-sectional polisher (IB-09020, JEOL). The cross-sectional images were analyzed at a low voltage of 2 kV using an EDS (XFlash, FlatQUAD, BRUKER) with high energy resolution to confirm the microstructure. The adhesive strength of the anode was evaluated using a SAICAS (DAIPLA WINTES Co., Ltd.). This process involved using a diamond blade to cut composite cathode samples to various depths: upper (25%), middle (50%), and lower (75%) of the electrode thickness. Horizontal and vertical forces were recorded while moving the blade vertically at $0.2 \mu\text{m s}^{-1}$ and horizontally at $2.0 \mu\text{m s}^{-1}$. Upon reaching the desired depth, the horizontal force was measured as a section was peeled off from the anode at a horizontal speed of $2.0 \mu\text{m s}^{-1}$. The inner framework and distribution of components and pores in the 3D-reconstructed images of each electrode were analyzed using an X-ray microscope (3D-XRM, CMOS2, BRUKER). To determine the T_m of the PVDF-HFP binder, DSC measurements were performed on a fully dried sample within a temperature range of -50 to $350 \text{ }^\circ\text{C}$ at a heating rate of $10 \text{ }^\circ\text{C min}^{-1}$. To evaluate the wettability of the electrolyte, a contact angle device was used to measure the angle 5 and 10 s after the electrolyte dropped onto the electrode. The resistance of each electrode was measured using an electrode resistance measurement system (RM2610, HIOKI) by applying a CC and measuring the voltage generated on the surface through 46 tip probes. This allowed for the analysis of the resistance between the current collector and the interface, as well as the bulk volume resistivity and surface resistance. The specific surface area and pore size distribution were analyzed using the Brunauer-Emmett-Teller (BET, Tristar II 3020, MICROMERITICS) method.

Cell Assembly: In the coin half cell, the prepared anode electrode was cut into 12 mm diameter discs in a dry room (dew point below $-50 \text{ }^\circ\text{C}$). A 16 mm diameter, 0.2 T Li metal (Honjo metal) was used as the counter electrode and reference electrode. The coin cell was assembled using a polyethylene (PE) separator and an electrolyte mixture of 1.0 M LiPF_6 in

EC/ethylene methyl carbonate (EC/EMC 3/7, w/w) with 2 wt.% vinylene carbonate (VC), along with the DCE and SCE electrodes (target current density: 6.5 mAh cm^{-2} , electrode density 1.5 g cm^{-3}). The coin full cell used the same separator and electrolyte as the half cell and was paired with an NCM dry cathode at an N/P ratio of 1.13. A single-layer pouch full cell was manufactured by packaging a 30.5 mm x 39.5 mm anode electrode and a 28.5 mm x 37.5 mm cathode electrode in an aluminum pouch film.

Electrochemical Measurement: For the evaluation of all cells, aging was conducted for 48 h in a $25 \text{ }^\circ\text{C}$ chamber, followed by testing using a battery cycler (WBCS 3000, WonATech). The formation of the coin half-cell was carried out with three charge/discharge cycles at 0.1 C, with cutoffs between 0.005 and 1.5 V. After formation, the charge rate evaluation involved performing three cycles of CC charging at 0.2 C, 0.5 C, 1.0 C, and 2.0 C, followed by CV charging at 0.005 C, with discharging at 0.2 C. Cyclic voltammetry (CV) was conducted at a scan rate of 0.1 mV s^{-1} . Both coin full cells and pouch full cells also underwent 48 h of aging in a $25 \text{ }^\circ\text{C}$ chamber and were evaluated in the voltage range of 2.5–4.3 V versus Li/Li^+ . The discharge rate was assessed by performing three cycles each at discharge rates ranging from 0.2 to 3.0 C, with charging at 0.2 C, followed by capacity recovery at 0.2 C. Electrochemical impedance spectroscopy (EIS, VSP, Biologic) measurements were performed in the frequency range from 200 kHz to 1 mHz with an amplitude of 10 mV. The GITT was conducted at 0.1 C with 10-min pulses and 1-h rest periods within the same voltage range. Cycle performance was evaluated by charging at a rate of 0.5 C using CC/CV and discharging at 0.5 C CC.

Supporting Information

Supporting Information is available from the Wiley Online Library or from the author.

Acknowledgements

J.-W.M. and K.-H.H. contributed equally to this work. This work was supported by the Industrial Technology Innovation Program (RS-2022-00155854 and 20007045) funded by the Ministry of Trade, Industry & Energy (MOTIE, Korea).

Conflict of Interest

The authors declare no conflict of interest.

Data Availability Statement

The data that support the findings of this study are available from the corresponding author upon reasonable request.

Keywords

dry processes, graphite anode, lithium-ion batteries, polymer binders

Received: December 23, 2024

Revised: February 20, 2025

Published online:

- [1] A. Masias, J. Marcicki, W. A. Paxton, *ACS Energy Lett.* **2021**, *6*, 621.
- [2] S. Chen, F. Dai, M. Cai, *ACS Energy Lett.* **2020**, *5*, 3140.
- [3] J. Li, J. Fleetwood, W. B. Hawley, W. Kays, *Chem. Rev.* **2022**, *122*, 903.
- [4] D. L. Wood, J. Li, C. Daniel, *J. Power Sources* **2015**, *275*, 234.
- [5] H. C. Kim, T. J. Wallington, R. Arsenault, C. Bae, S. Ahn, J. Lee, *Environ. Sci. Technol.* **2016**, *50*, 7715.
- [6] H. C. Kim, S. Lee, T. J. Wallington, *Environ. Sci. Technol.* **2023**, *57*, 11834.
- [7] D. L. Wood, M. Wood, J. Li, Z. Du, R. E. Ruther, K. A. Hays, N. Muralidharan, L. Geng, C. Mao, I. Belharouak, *Energy Storage Mater.* **2020**, *29*, 254.
- [8] Q. Wu, J. P. Zheng, M. Hendrickson, E. J. Plichta, *MRS Adv.* **2019**, *4*, 857.
- [9] Y. Li, Y. Wu, Z. Wang, J. Xu, T. Ma, L. Chen, H. Li, F. Wu, *Mater. Today* **2022**, *55*, 92.
- [10] K.-H. Pettinger, W. Dong, *J. Electrochem. Soc.* **2016**, *164*, A6274.
- [11] M. Al-Shroofy, Q. Zhang, J. Xu, T. Chen, A. P. Kaur, Y.-T. Cheng, *J. Power Sources* **2017**, *352*, 187.
- [12] D. L. Wood, J. D. Quass, J. Li, S. Ahmed, D. Ventola, C. Daniel, *Drying Technol.* **2017**, *36*, 234.
- [13] R. Sahore, D. L. Wood, A. Kukay, K. M. Grady, J. Li, I. Belharouak, *ACS Sustainable Chem. Eng.* **2020**, *8*, 3162.
- [14] Y. Zhang, S. Lu, Z. Wang, V. Volkov, F. Lou, Z. Yu, *Renewable Sustainable Energy Rev.* **2023**, *183*, 113515.
- [15] S. Jaiser, M. Müller, M. Baunach, W. Bauer, P. Scharfer, W. Schabel, *J. Power Sources* **2016**, *318*, 210.
- [16] Y. S. Zhang, N. E. Courtier, Z. Zhang, K. Liu, J. J. Bailey, A. M. Boyce, G. Richardson, P. R. Shearing, E. Kendrick, D. J. L. Brett, *Adv. Energy Mater.* **2021**, *12*, 2102233.
- [17] W. Yao, M. Chouchane, W. Li, S. Bai, Z. Liu, L. Li, A. X. Chen, B. Sayahpour, R. Shimizu, G. Raghavendran, M. A. Schroeder, Y.-T. Chen, D. H. S. Tan, B. Sreenarayanan, C. K. Waters, A. Sichter, B. Gould, D. J. Kountz, D. J. Lipomi, M. Zhang, Y. S. Meng, *Energy Environ. Sci.* **2023**, *16*, 1620.
- [18] M. Ryu, Y. K. Hong, S. Y. Lee, J. H. Park, *Nat. Commun.* **2023**, *14*, 13116.
- [19] Y. Lu, C.-Z. Zhao, H. Yuan, J.-K. Hu, J.-Q. Huang, Q. Zhang, *Matter* **2022**, *5*, 876.
- [20] J. Schnell, T. Günther, T. Knoche, C. Vieider, L. Köhler, A. Just, M. Keller, S. Passerini, G. Reinhart, *J. Power Sources* **2018**, *382*, 160.
- [21] Y. Kuang, C. Chen, D. Kirsch, L. Hu, *Adv. Energy Mater.* **2019**, *9*, 1901457.
- [22] B. Ludwig, Z. Zheng, W. Shou, Y. Wang, H. Pan, *Sci. Rep.* **2016**, *6*, 23150.
- [23] X. Yang, K. Doyle-Davis, X. Gao, X. Sun, *eTransportation* **2022**, *11*, 100152.
- [24] J. Wang, D. Shao, Z. Fan, C. Xu, H. Dou, M. Xu, B. Ding, X. Zhang, *ACS Appl. Mater. Interfaces* **2024**, *16*, 26209.
- [25] F. Wu, M. Liu, Y. Li, X. Feng, K. Zhang, Y. Bai, X. Wang, C. Wu, *Electrochem. Energy Rev.* **2021**, *4*, 382.
- [26] H. Kim, J. H. Lim, T. Lee, J. An, H. Kim, H. Song, H. Lee, J. W. Choi, J. H. Kang, *ACS Energy Lett.* **2023**, *8*, 3460.
- [27] H. Oh, G.-S. Kim, B. U. Hwang, J. Bang, J. Kim, K.-M. Jeong, *Chem. Eng. J.* **2024**, 491.
- [28] T. Qin, H. Yang, Q. Li, X. Yu, H. Li, *Ind. Chem. Mater.* **2024**, *2*, 191.
- [29] Z. Wei, D. Kong, L. Quan, J. He, J. Liu, Z. Tang, S. Chen, Q. Cai, R. Zhang, H. Liu, K. Xu, L. Xing, W. Li, *Joule* **2024**, *8*, 1350.
- [30] N.-S. Choi, S.-Y. Ha, Y. Lee, J. Y. Jang, M.-H. Jeong, W. C. Shin, M. Ue, *J. Electrochem. Sci. Technol.* **2015**, *6*, 35.
- [31] S. Han, E.-H. Noh, S. Chae, K. Kwon, J. Lee, J.-S. Woo, S. Park, J. W. Lee, P. J. Kim, T. Song, W.-J. Kwak, J. Choi, *J. Energy Storage* **2024**, *96*.
- [32] G. Li, R. Xue, L. Chen, *Solid State Ionics* **1996**, *90*, 221.
- [33] T. Lee, J. An, W. J. Chung, H. Kim, Y. Cho, H. Song, H. Lee, J. H. Kang, J. W. Choi, *ACS Appl. Mater. Interfaces* **2024**, *16*, 8930.
- [34] Y. Suh, J. K. Koo, H.-j. Im, Y.-j. Kim, *Chem. Eng. J.* **2023**, *476*, 146299.
- [35] W. J. Chang, G. H. Lee, Y. J. Cheon, J. T. Kim, S. I. Lee, J. Kim, M. Kim, W. I. Park, Y. J. Lee, *ACS Appl. Mater. Interfaces* **2019**, *11*, 41330.
- [36] B. Son, M. H. Ryou, J. Choi, T. Lee, H. K. Yu, J. H. Kim, Y. M. Lee, *ACS Appl. Mater. Interfaces* **2014**, *6*, 526.
- [37] O. O. Taiwo, D. P. Finegan, J. Gelb, C. Holzner, D. J. L. Brett, P. R. Shearing, *Chem. Eng. Sci.* **2016**, *154*, 27.
- [38] K. Park, S. Myeong, D. Shin, C.-W. Cho, S. C. Kim, T. Song, *J. Ind. Eng. Chem.* **2019**, *71*, 270.
- [39] M. P. Lautenschlaeger, B. Prifling, B. Kellers, J. Weinmiller, T. Danner, V. Schmidt, A. Latz, *Batteries Supercaps* **2022**, *5*, 202200090.
- [40] K. Lee, Y. Jo, J. Seok Nam, H. Yu, Y.-j. Kim, *Chem. Eng. J.* **2024**, 487.
- [41] R. Morasch, J. Landesfeind, B. Suthar, H. A. Gasteiger, *J. Electrochem. Soc.* **2018**, *165*, A3459.
- [42] H. Choi, D. Moon, J. Sheem, J. K. Koo, S. Hong, S.-M. Oh, Y.-j. Kim, *J. Electrochem. Soc.* **2023**, 170.
- [43] K. M. Kim, J. W. S., C. I. J., C. S. H., *J. Power Sources* **1999**, *83*, 108.
- [44] Y. H. Kwon, M. M. Huie, D. Choi, M. Chang, A. C. Marschilok, K. J. Takeuchi, E. S. Takeuchi, E. Reichmanis, *ACS Appl. Mater. Interfaces* **2016**, *8*, 3452.
- [45] J. Kang, J. Lim, H. Lee, S. Park, C. Bak, Y. Shin, H. An, M. Lee, M. Lee, S. Lee, B. Choi, D. Kang, S. Chae, Y. M. Lee, H. Lee, *Adv. Sci.* **2024**, *11*, 2403071.
- [46] K.-H. Chen, M. J. Namkoong, V. Goel, C. Yang, S. Kazemiabnavi, S. M. Murtuza, E. Kazyak, J. Mazumder, K. Thornton, J. Sakamoto, N. P. Dasgupta, *J. Power Sources* **2020**, *471*, 228475.
- [47] R. Morasch, H. A. Gasteiger, B. Suthar, *J. Electrochem. Soc.* **2024**, *165*, A3459.
- [48] P. Niehoff, S. Passerini, M. Winter, *Langmuir* **2013**, *29*, 5806.
- [49] I. Källquist, R. L. e Ruyet, H. Liu, R. Mogensen, M.-T. Lee, K. Edström, A. J. Naylor, *J. Mater. Chem. A* **2022**, *10*, 19466.